

## A Comparison of SIR-B Directional Ocean Wave Spectra with Aircraft Scanning Radar Spectra

R. C. BEAL, F. M. MONALDO, D. G. TILLEY, D. E. IRVINE, E. J. WALSH, F. C. JACKSON, D. W. HANCOCK III, D. E. HINES, R. N. SWIFT, F. I. GONZALEZ, D. R. LYZENGA, L. F. ZAMBRESKY

Directional ocean wave spectra derived from Shuttle Imaging Radar-B (SIR-B) L-band imagery collected off the coast of southern Chile on 11 and 12 October 1984 were compared with independent spectral estimates from two airborne scanning radars. In sea states with significant wave heights ranging from 3 to 5 meters, the SIR-B-derived spectra at 18° and 25° off nadir yielded reasonable estimates of wavelengths, directions, and spectral shapes for all wave systems encountered, including a purely azimuth-traveling system. A SIR-B image intensity variance spectrum containing predominantly range-traveling waves closely resembles an independent aircraft estimate of the slope variance spectrum. The prediction of a U.S. Navy global spectral ocean wave model on 11 October 1984 exhibited no significant bias in dominant wave number but contained a directional bias of about 30° with respect to the mean of the aircraft and spacecraft estimates.

THE ABILITY TO MAKE ACCURATE global estimates of the directional wave energy spectrum of the ocean has been a goal of oceanographers for at least two decades (1). Such a capability would revolutionize our knowledge of global wave climatology, and the validation, refinement, and periodic updating of existing ocean wave forecast models would immediately become a practical possibility.

Few techniques exist for estimating the directional wave spectrum. Directional wave rider buoys, developed in the 1960's, have been widely utilized and are useful for characterizing unimodal wave systems at a single location. However, with directional buoys it is difficult to measure spectral widths, and such measurements become confused in the presence of bimodal wave systems traveling in different directions. Aircraft stereopho-

tography is sometimes useful, but it is limited by clouds and is not a candidate for a global all-weather operational system.

In 1978, the Seasat synthetic aperture radar (SAR) obtained the first high-resolution radar images of the ocean from space, demonstrating its potential as a global monitoring system for directional energy spectra. However, the SAR-measured ocean backscatter is only indirectly related to the ocean wave height or energy. Moreover, some theoretical models predict that highly nonlinear imaging mechanisms can dominate the transformation from SAR backscatter to ocean height (2), contaminating the SAR image to such an extent that inversion to an absolute energy spectrum would become impossible. Although such catastrophic situations have not been observed in any of the published Seasat SAR data, Seasat spectra were affected by azimuth (along-track) filtering, which acted to rotate (and sometimes obliterate) wave systems having a significant azimuth component (3, 4).

The details of the SAR azimuth contamination depend upon the hydrodynamic and electromagnetic properties of the moving sea surface (5); independent of these details, however, the degree of contamination is directly proportional to the range-to-velocity ratio ( $R/V$ ) of the radar platform. The  $R/V$  ratio for Seasat at an altitude of 800 km and an off-nadir angle of 20° was about 130 seconds;  $R/V$  for Shuttle Imaging Radar-B (SIR-B) at 230-km altitude and a similar off-nadir angle was only 35 seconds. Therefore, the spectral contamination that was evident in Seasat SAR spectra, whatever its exact cause in terms of scatterer motion, should

Table 1. Summary of estimated and predicted wave systems for 11 and 12 October 1984. Listed are wave number  $k$  and direction  $\theta$  of all detected wave systems along with their associated spectral widths  $\Delta k$  and  $\Delta\theta$ .

Source	Primary wave system*					Secondary wave system†			
	$H_s$ (m)	$k$ (rad/m)	$\Delta k$ (rad/m)	$\theta$ (deg)	$\Delta\theta$ (deg)	$k$ (rad/m)	$\Delta k$ (rad/m)	$\theta$ (deg)	$\Delta\theta$ (deg)
<i>12 October</i>									
SCR	3.4	0.017	0.008	103	50				
ROWS	3.9	0.017	0.010	98	52	0.047	0.013	204	30
SIR-B‡	3.5	0.019	0.012	97	70	0.048	0.014	205	30
<i>11 October</i>									
ROWS	4.8	0.024	0.013	146	39	0.052	0.012	143	32
SIR-B‡	4.0	0.025	0.012	143	33	0.052	0.014	150	30
GSOWM (55°S)	3.0	0.025	0.023	172	60				
GSOWM (50°S)	4.9	0.023	0.025	135	77				

\*Primary wave parameters were estimated from integrated variance spectra, with  $k, \theta$  centered at about half-power ( $\Delta k, \Delta\theta$ ) points. †Secondary wave parameters were estimated with spectral cuts through the slope spectra. ‡Estimates of  $H_s$  for normalizing SIR-B spectra were obtained from an aircraft nadir-looking radar altimeter.

R. C. Beal, F. M. Monaldo, D. G. Tilley, D. E. Irvine, Johns Hopkins University Applied Physics Laboratory, Laurel, MD 20707.

E. J. Walsh, F. C. Jackson, D. W. Hancock III, D. E. Hines, NASA Goddard Space Flight Center, Greenbelt, MD 20771.

R. N. Swift, EG&G Analytical Services Center, Inc., Pocomoke City, MD 21851.

F. I. Gonzalez, National Oceanic and Atmospheric Administration Pacific Marine Environmental Laboratory, Seattle, WA 98115.

D. R. Lyzenga, Environmental Research Institute of Michigan, Ann Arbor, MI 48107.

L. F. Zambresky, Fleet Numerical Oceanography Center, Monterey, CA 93940.

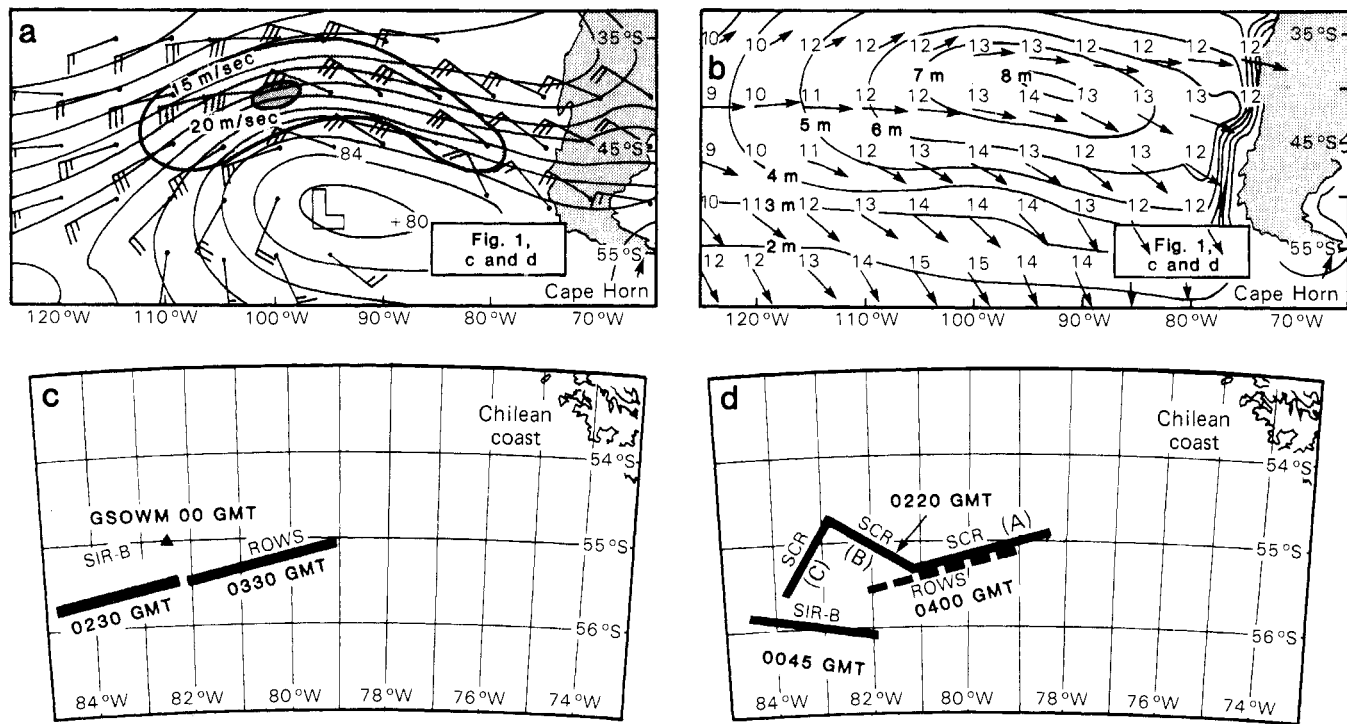


Fig. 1. (a) GSOWM input winds for 1800 GMT, 10 October 1984. The storm was intense with peak winds of 20 m/sec. The barbs show wind speed in knots. (b) GSOWM output waves for 00 GMT, 11 October. Shown are  $H_s$  (in meters) and the period and direction of the primary wave system. (c)

SIR-B and ROWS measurement locations for 11 October with respect to the nearest GSOWM grid point. (d) SIR-B, ROWS, and SCR measurement locations for 12 October. GSOWM was inoperative.

have been reduced by nearly a factor of 4 in SIR-B spectra.

To confirm the anticipated improvement in SIR-B estimates of directional wave spectra, we conducted a series of nearly simultaneous and coincident aircraft underflights off the coast of southern Chile, over a region in which the expected significant wave height ( $H_s$ ) exceeded 4 m. The aircraft, a NASA P-3, contained two independent scanning radars to estimate the directional energy spectrum: a raster-scanning surface contour radar (SCR) and a conically scanning radar ocean wave spectrometer (ROWS). The SCR obtains a high-spatial-resolution surface height or energy map directly (6) but requires multiple flight directions to maximize spectral resolution. The ROWS obtains a high-spectral-resolution surface slope spectrum (7), from which a surface height or energy spectrum can be derived.

SIR-B overpasses of interest occurred between 00 GMT and 03 GMT from 8 October through 12 October 1984. During this period, the weather patterns produced a range of  $H_s$  values from 1.5 to 5 m in the measurement region. We discuss here the initial results for 11 and 12 October, for which the SIR-B off-nadir angles were 25° and 18°, respectively, and  $H_s$  values, estimated from the aircraft nadir-looking altimeter, were about 4 and 3.5 m, respectively.

On both days, the weather, as analyzed by

the U.S. Fleet Numerical Oceanography Center (FNOC), was dominated by an easterly traveling low-pressure system containing a broad area of winds with velocities of 15 to 20 m/sec in its northern two quadrants (Fig. 1a). The resulting wave field predicted by the FNOC global spectral ocean wave model (GSOWM) (8) contained a region of waves characterized by  $H_s$  values of 8 m, a 14-second dominant period (or 300-m dominant wavelength) emanating from a small energetic core, and a travel direction generally to the east-southeast (Fig. 1b). Ahead of this core and to the south, the source winds weakened as they turned more northerly. The resultant waves also turned and gradually became less energetic with shorter period.

On 11 October, SIR-B and both aircraft scanning radars were operating, although the SCR was activated too briefly to obtain reliable spectra. The slope spectra were bimodal, according to ROWS estimates obtained over more than a 100-km span (Fig. 1c). SIR-B spectra reported here were obtained about 1 hour before and 50 km to the west of the ROWS spectra. The GSOWM forecast for 00 GMT, 11 October, predicted a single dominant wave system arriving in the measurement region from the north-northeast, with a dominant period of 12 seconds (215-m wavelength) and  $H_s \sim 3.0$  m (Fig. 1b).

On 12 October, SIR-B and both aircraft

scanning radars were operating, but the GSOWM estimates were unavailable because of a local power failure. To compensate for their relatively poor cross-track resolution, we obtained SCR spectra by combining data from three separate flight directions (Fig. 1d). The resulting synthesis of a single composite spectrum contains improved spectral resolution, albeit with the assumption of spatial homogeneity over the entire SCR flight path. SIR-B spectra were obtained within 100 km to the south and west of and 2 to 4 hours before the aircraft measurements.

Spectral comparisons and estimates for both days are summarized in Figs. 2 and 3 and in Table 1. Since the data set for 12 October affords a three-way comparison of completely independent spectral estimates, we consider this our primary data set. Figure 2, a, c, and e, illustrates the "derived" character of each of the corresponding height variance spectra (Fig. 2, b, d, and f). The synthesized SCR spectrum (Fig. 2b) is derived from individual (Fig. 2a) lower resolution spectra obtained along each of three flight lines. In contrast to the case for ROWS and SAR, the SCR directional ambiguity can be removed if one compares the differential Doppler effects resulting from aircraft velocity along each of the three flight lines (6). ROWS directly measures a slope variance spectrum (Fig. 2c), from which a height variance spectrum (Fig. 2d) is ob-

tained through a  $1/k^2$  (where  $k = 2\pi/\text{wavelength}$ ) transformation. Similarly, for a first approximation we treat the SAR image spectra as slope variance spectra, after appropriate corrections for the instrument transfer function (3, 4).

A corrected SIR-B image intensity variance spectrum is shown in Fig. 2e, and a derived spectrum, obtained by multiplying the corrected spectrum by  $1/k^2$ , is shown in Fig. 2f. If Fig. 2e were indeed a pure slope variance spectrum, then Fig. 2f would represent a pure height variance spectrum. For azimuth-traveling waves, however, there is no tilt mechanism, and other imaging effects must govern. If velocity bunching dominates (2, 5), the SAR intensity variance spectrum in the azimuth direction will be proportional to the product of  $k^3$  (rather than  $k^2$ ) and the height variance spectrum, at least for wavelengths greater than 100 m, which are of interest here. The slight bias of SIR-B spectra toward higher azimuth wave numbers (Fig. 2g and Table 1), which would result from a  $k^3$  dependence, suggests that the velocity-bunching mechanism may well be operating. Even granting this single caveat, we appear to have three independent and remarkably consistent measures of nearly all the principal features of the spectrum on 12 October. Weak secondary systems at the higher wave numbers were detected by both ROWS and SIR-B but not by SCR. Apparently the two slope-responding instruments are relatively more sensitive to energy at the higher wave numbers. The integrated height variance spectra (Fig. 2, g and h) are given in absolute units. The SIR-B spectra were normalized with the use of estimates of  $H_s$  (Table 1) obtained with the aircraft nadir-looking altimeter, which is similar to the instrument flown on Seasat in 1978.

On 11 October, nearly coincident ROWS and SIR-B spectra (Fig. 3, a and c) were also highly correlated, both showing a bimodal system separated in wavelength by a factor of 2, with each system traveling in a nearly identical direction ( $\pm 180^\circ$ ). Transformations of the spectra by  $1/k^2$  (Fig. 3, b and d) greatly attenuated the short wave system, but it still remained evident as extended tails in the corresponding integrated spectra of Fig. 3g.

SAR seems to be responding directly to the surface slope, a result that in this case has good theoretical basis (9) because of the fortuitous geometry and local wind conditions. The wave field consists of two nearly range-traveling systems for which the local wind is also nearly range-traveling. This geometry is very close to the ideal situation for which the amplitude modulation of the 30-cm Bragg scatterers is controlled by the

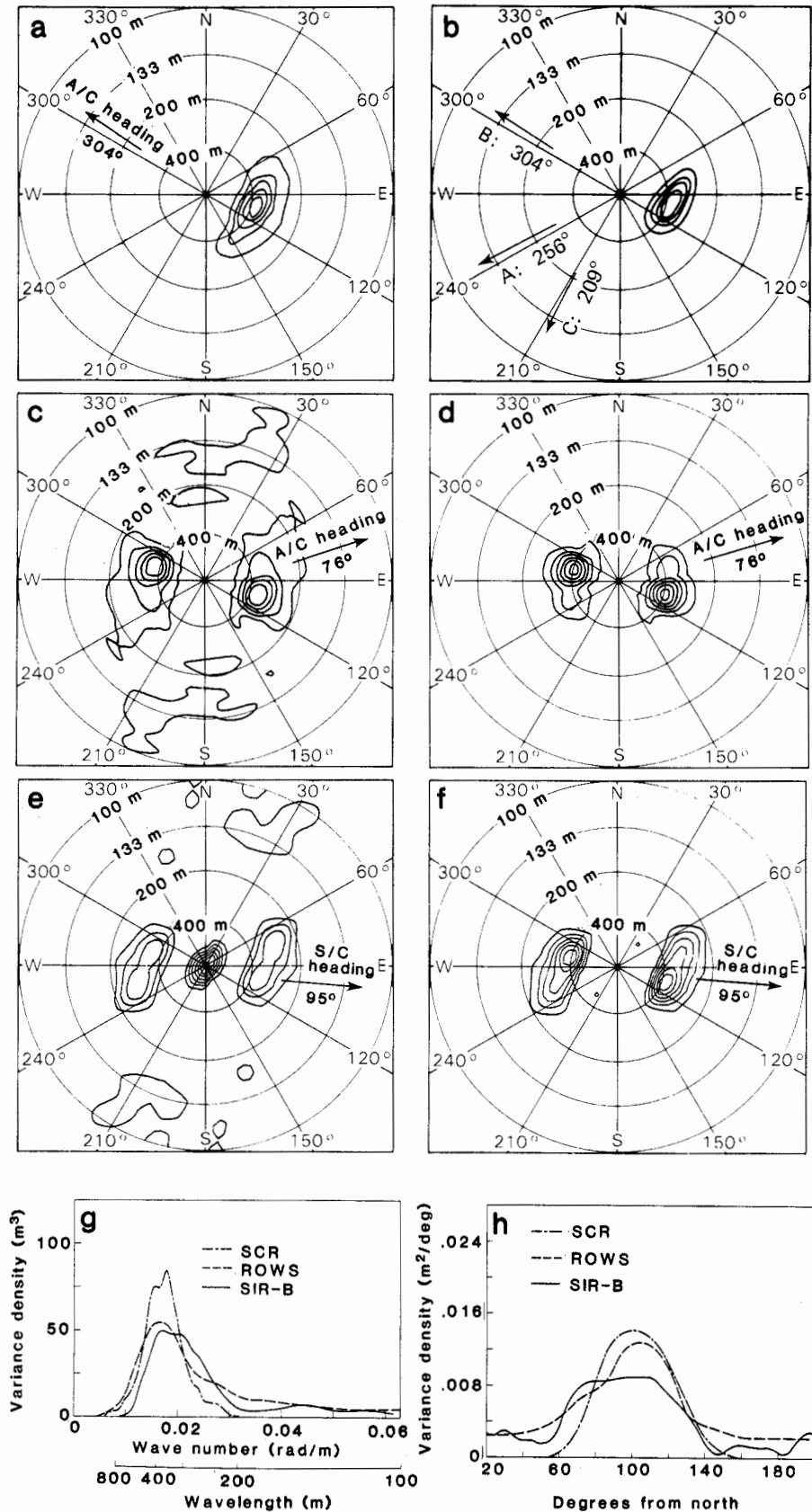


Fig. 2. Wave number spectra for 12 October. (a) SCR height variance spectrum along flight line B (Fig. 1d); A/C heading, aircraft heading. (b) SCR height variance spectrum from flight lines A, B, and C (Fig. 1d). (c) ROWS slope variance spectrum (55.5°S, 81.5°W, 0400 GMT). (d) ROWS height variance spectrum (55.5°S, 81.5°W, 0400 GMT). (e) SIR-B intensity variance spectrum (56.0°S, 82.0°W, 0045 GMT); S/C heading, spacecraft heading. (f) SIR-B intensity variance spectrum multiplied by  $1/k^2$  (56.0°S, 82.0°W, 0045 GMT). (g) Nondirectional integrated variances. (h) Directional integrated variances.

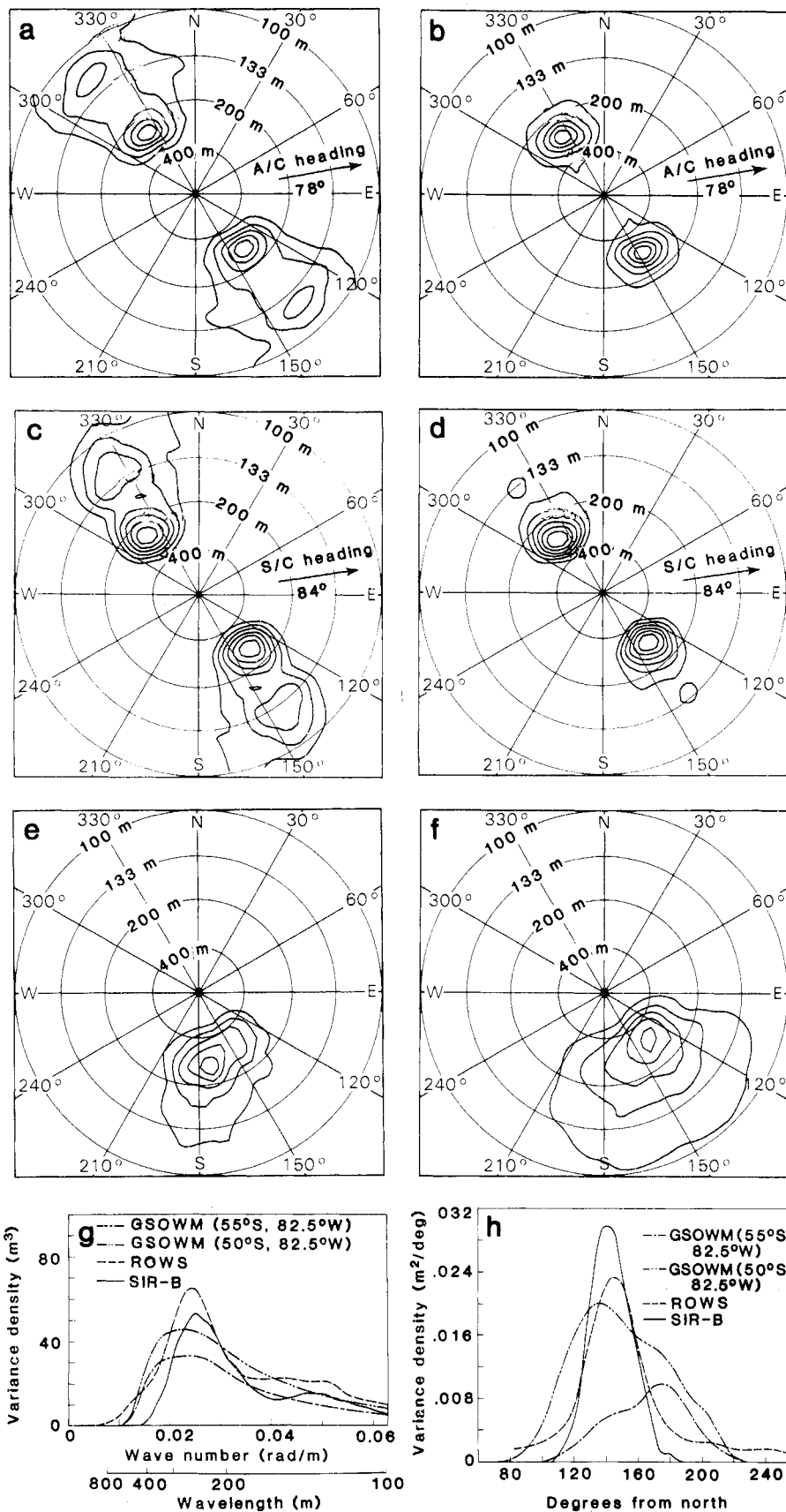


Fig. 3. Wave number spectra for 11 October. (a) ROWS slope variance spectrum (55.3°S, 81.2°W, 0330 GMT). (b) ROWS height variance spectrum (55.3°S, 81.2°W, 0330 GMT). (c) SIR-B intensity variance spectrum (55.5°S, 82.5°W, 0230 GMT). (d) SIR-B intensity variance spectrum multiplied by  $1/k^2$  (55.5°S, 82.5°W, 0230 GMT). (e) GSOWM height variance forecast (55.0°S, 82.5°W, 00 GMT). (f) GSOWM height variance forecast (50.0°S, 82.5°W, 00 GMT). (g) Nondirectional integrated variances. (h) Directional integrated variances.

action-conserving straining of the long waves and their local tilt. Because the secondary system is slightly stronger in the SIR-B slope variance spectrum, the corresponding nondirectional height variance spectrum has an extended high wave number tail. Differences between ROWS and SIR-B estimates of the secondary system probably are not significant, since on scales of 50 km and 1 hour the ocean itself is variable to the same order.

Figure 3e shows the GSOWM prediction about 50 km north of the location of the SIR-B estimate and about 2½ hours earlier (see Fig. 1c). The model prediction is in good agreement with both SIR-B and ROWS results in its estimate of the dominant peak, but the mean propagation direction is rotated about 30° toward the south. Some 500 km to the north (Fig. 3f), because the wave field exhibited a rapid turning and strengthening (Fig. 1b), the GSOWM agreement with the measurements to the south was much better. Apparently, a displacement of the model source wind field of about 400 km to the south would minimize the discrepancy and would also tend to reconcile the model underestimates of  $H_s$  (3 m predicted versus about 4 m measured). Integrated versions of all spectra (Fig. 3, g and h) indicate a tendency for broadening in GSOWM with respect to both ROWS and SIR-B estimates.

The promise of a shuttle-altitude SAR (in conjunction with a nadir-looking altimeter) for giving operationally useful estimates of surface wave directional energy spectra is strengthened considerably by these results. SIR-B observed all primary and secondary wave systems that were detected by either SCR or ROWS, including a nearly pure azimuth-traveling wave system. There was no evidence of nonlinearities for any wave orientation, and interpretation of the range component of SAR spectra as slope spectra seems valid within the accuracy of our comparisons. In the azimuth direction, other mechanisms must dominate the imaging process, although even these are reasonably linear for waves longer than 100 m with this favorable SIR-B geometry (230-km altitude, 18° to 25° off nadir).

For example, the Alpers "nonlinearity parameter" (2) has a maximum value of ~0.2 for our data set, an indication that the velocity-bunching effect is well within the linear region, even for the relatively large wave heights encountered. Also for our data, the expected "azimuth cutoff" wavelength ( $\lambda_c$ ) is approximately 70 m, much shorter than the observed wavelengths. Our results therefore appear to be consistent with both SAR imaging theory and the Seasat experience. The wave-detecting capa-

bility of SIR-B, with its small  $R/V$  ratio, was substantially better than that of Seasat.

The practical utility of satellite-derived directional wave spectra (from either SAR or ROWS) for assimilation into operational wave models is reinforced by our results, although a low-altitude (<300 km) orbit will be necessary to achieve practical SAR imaging of azimuth-traveling waves. These results also indicate that the dominant wave number predicted by GSOWM was accurate but that the dominant wave direction was in

disagreement with the independent estimates by about 30°.

#### REFERENCES AND NOTES

1. G. C. Ewing, Ed., *Oceanography from Space* (Woods Hole Oceanographic Institution Report NASA-CR-64164, Woods Hole, MA, 1965).
2. W. Alpers, *J. Geophys. Res.* **88**, 1745 (1983).
3. R. C. Beal *et al.*, *ibid.*, p. 1761.
4. R. C. Beal *et al.*, *ibid.*, in press.
5. K. Hasselmann *et al.*, *ibid.* **90**, 4659 (1985).
6. E. J. Walsh *et al.*, *J. Phys. Oceanogr.* **15**, 566 (1985).
7. F. C. Jackson, W. T. Walton, C. Y. Peng, *J. Geophys. Res.* **90**, 1005 (1985).
8. R. M. Clancy *et al.*, *Bull. Am. Meteorol. Soc.*, in press.

9. O. M. Phillips, in *Spaceborne Synthetic Aperture Radar for Oceanography*, R. C. Beal, P. S. DeLeonibus, I. Katz, Eds. (Johns Hopkins Press, Baltimore, 1981), p. 24.
10. We are indebted to the government of Chile for vital aircraft logistic and meteorological support, to the government of Argentina for alternate landing privileges, to the NASA P-3 crew for their precision underflights, and to the California Institute of Technology Jet Propulsion Laboratory SIR-B team for their dedicated mission support and timely SAR image-processing. This work was supported by the National Aeronautics and Space Administration and the Office of Naval Research.

5 August 1985; accepted 21 February 1986

## pH-Induced Metabolic Transitions in *Artemia* Embryos Mediated by a Novel Hysteretic Trehalase

STEVEN C. HAND\* AND JOHN F. CARPENTER†

Gastrula-stage embryos of the brine shrimp *Artemia* undergo reversible transitions between metabolically active and dormant states that are promoted by changes in intracellular pH. A macromolecular mechanism for this suppression of energy metabolism that involves regulation of the enzyme trehalase is reported here. Isolated trehalase from these embryos existed in two active forms that interconverted when exposed to physiological transitions in pH. This hysteretic interconversion was reversible, required minutes for completion, and involved a change in enzyme polymerization. The two states differed twofold in molecular size and were distinguishable electrophoretically. Compared to the smaller species, the polymerized form was strongly inhibited by acidic pH, adenosine 5'-triphosphate, and the substrate trehalose. Thus, the shift in assembly equilibrium toward the aggregated enzyme caused by pH values less than or equal to 7.4 may mediate the arrest of trehalase-fueled metabolism and respiration during dormancy in this cryptobiotic organism.

THE ROLE OF INTRACELLULAR pH ( $pH_i$ ) in the suppression and activation of cellular metabolism is becoming increasingly well documented for both unicellular and multicellular organisms. Entry into and exit from dormancy is often accompanied by various amounts of acidification and alkalinization of the cellular milieu (1). In the brine shrimp *Artemia*, hydrated embryos (cysts) undergo reversible transitions between a metabolically active state of aerobic development and a cryptobiotic condition termed anaerobic dormancy (2); these transitions are accompanied by large shifts in  $pH_i$  from values of or above 7.9 to 6.3 (3).  $pH_i$  is the fundamental regulator for the transitions between these very different metabolic states (4). Acidification of the  $pH_i$  of aerobically developing cysts to 6.8 by exposure to elevated levels of  $CO_2$  (aerobic acidosis) induces a quiescent condition comparable to anaerobic dormancy, as judged by suppression of hatching and oxygen consumption; removal of  $CO_2$  reverses the effect. The mechanism by which this proton signal is coupled to the observed physiological response is the focus of our study.

In *Artemia* cysts, preemergence development and metabolism is fueled exclusively by the disaccharide trehalose (5, 6), and transitions in  $pH_i$  directly and reversibly arrest carbohydrate metabolism in these embryos (7). This evaluation (7) of carbohydrate levels with crossover point theory (8) revealed that the conversion of trehalose to glucose is the first nonequilibrium reaction reversibly inhibited by  $pH_i$ ; during both aerobic acidosis and anaerobic dormancy. If one assumes that all mobilized trehalose that is not converted to glycerol or glycogen is completely oxidized under aerobic conditions (6), the 95 percent shutdown of trehalose catabolism in aerobic acidosis (7) quantitatively accounts for the large suppression of oxygen consumption (4) seen under these conditions.

Thus, any mechanism proposed for the pH-induced metabolic transitions in *Artemia* embryos must explain the proton modulation of the trehalase reaction. We suggest that the proton-dependent shutdown of trehalase mobilization, and thereby energy metabolism, in these embryos results from a shift in assembly equilibrium of a novel, hysteretic trehalase. As originally defined

(9), hysteretic enzymes have certain kinetic or molecular characteristics that respond slowly to a rapid change in the concentration of a ligand (for example, protons in the case of *Artemia* trehalase). The change in ligand concentration presumably induces a conversion of one enzyme form to another form that has different properties.

Our initial examination of crude trehalase preparations from hydrated cysts (Great Salt Lake, Utah, population) using nondenaturing polyacrylamide gel electrophoresis (PAGE) revealed two distinct, catalytically active forms of the enzyme (Fig. 1A) that could be visualized with substrate-specific activity staining (10). Multiple molecular species of trehalase are also seen in electrophoretic studies of the enzyme from insects and cellular slime mold (11). Elution profiles of *Artemia* trehalase activity from hydroxylapatite columns suggested that the two forms were interconvertible. We, therefore, separated this chromatographically enriched mixture of trehalase forms that exist at pH 7.0 (12) by electrophoresis on preparative slab gels, cut the slow-migrating form (which was well separated from the more mobile band) from the gel, and extracted it from the acrylamide matrix with buffer. Electrophoresis of the eluted trehalase on analytical gels again revealed the presence of both the slow- and fast-migrating forms (Fig. 1B) at the same ratio seen in the preparative gel; thus the slow-migrating molecular species could give rise to the fast-migrating form.

The first evidence suggesting that the molecular interconversion of trehalase was reversible and directly promoted by alter-

Department of Biology, University of Southwestern Louisiana, Lafayette, LA 70504.

\*Present address: Department of Environmental, Population and Organismic Biology, University of Colorado, Boulder, CO 80309.

†Present address: Department of Zoology, University of California, Davis, CA 95616.